Collisionless Gas Flows over a Cylindrical or Spherical Object

Chunpei Cai,* Khaleel R. A. Khasawneh,† Hongli Liu,‡ and Mingjun Wei§
New Mexico State University, Las Cruces, New Mexico 88003-8001

This paper presents exact density, velocity components, and temperature solutions for collisionless gas flows over a cylinder or a sphere. Possible real applications may include collisionless gas flows over a hot wire inside a vacuum chamber and rarefied gas flows around an aerosol at very high altitude. At any point off the cylinder or the sphere, the local velocity distribution function consists of two pieces of Maxwellian distribution functions: one for the freestream, which is characterized by the freestream density n_0, temperature T_0, and velocity U_0; the other is characterized by density at the wall n_w and wall temperature T_w, where n_w is not constant at different surface locations. Directly integrating the distribution functions leads to the detailed flowfield solutions; the solutions are complex but exact. We performed numerical simulations with the direct simulation Monte Carlo method to validate these exact solutions. In general, the exact analytical and numerical results are virtually identical.

Nomenclature

f	=	velocity distribution function
Kn	=	Knudsen number
n	=	number density
n_x, n_y, n_z	=	local surface normal direction
P	=	macroscopic pressure
R	=	universal gas constant
r, θ	=	polar coordinate variables
S	=	speed ratio
T	=	macroscopic temperature
U, V, W	=	macroscopic average velocity
u, v, w	=	microscopic molecular velocity
X, Y, Z	=	point on the circular or spherical external boundary
x, y, z	=	point in flowfield
α	=	angle between freestream and local surface normal or specific position angle
ζ	=	angle between freestream and local surface normal
Ω	=	specific domain in velocity space

Subscripts

w	=	wall property
0	=	freestream macroscopic value

I. Introduction

COLLISIONLESS external flows over a cylindrical or spherical object have many applications. Examples include highly rarefied gas flows around 1) a very small pollen or a pollutant particle, 2) a lunar dust particle during a moon-landing mission, 3) an aerosol droplet at high altitude, 4) a fine metal powder particle during a thin-film deposition processing inside a vacuum chamber, 5) a meteoroid traveling in space, 6) a small cold sphere with absorption or condensation effects, 7) a spherical spacecraft in low earth orbit with outgassing effects, 8) a fine fiber of a dust mask, 9) a hot wire inside vacuum chambers [1], 10) a thin filament inside a low-pressure light bulb, or 11) cylindrical objects with sticking or absorption effects, for example, with cryogenic effects. The related aerodynamic coefficients are important for spacecraft design as well. The earliest work may date back to Epstein [2] and Kogan [3]; several more recent books discussed collisionless aerodynamics over a flat plate as well, such as those by Gombosi [4], Shen [5], and Bird [6]. Especially, Bird [6] discussed plate surface properties for collisionless flows with both diffuse and specular reflections, and the direct simulation Monte Carlo (DSMC) method is one appropriate numerical tool to simulate such of gas flows. Chen [7] discussed the surface drag and heat transfer for collisionless flows over a plate, a cylinder, and a small sphere. Sone provided some review comments on highly rarefied gas flows [8]. Recently, Loth [9] reviewed compressibility and rarefaction effects on drag over a small sphere. In the literature, almost all of the studies on collisionless flows over a cylinder or a sphere focused on the wall properties. It seems that the flowfield around a cylinder or a sphere should be very simple without any collision effects, but in the literature, there was no discussion on them; available research work in the literature concentrates on numerical simulations of the flowfield. For continuum incompressible potential flow situations, the flowfield solutions are very classical, but for the high-Knudsen-number situations, it seems there is no exact solution for these fundamental problems yet. The purpose of this paper is to provide the exact solutions for the collisionless gas flow over a cylinder or a sphere. As such, this paper complements the past studies on aerodynamic coefficients and heat transfer rate over a sphere or a cylinder in the literature. It is also worth mentioning that, for the 11 flow examples we listed here, some high-Knudsen-number flows are due to a low gas density, whereas some are from a small characteristic length. Not all high-Kn gas flows can be treated as collisionless or rarefied gas flows [10,11]. The high-Kn gas flow caused by very small characteristic length can only by treated as similar to the rarefied gas flow when the perfect gas assumption still stands. Fortunately, people have proven that such an assumption still works up to a high pressure, such as 5 atm for air [12,13]. Those works can be used to validate the working range of the current analytical solutions from this study.

In this study, we are about to use a relation between particle velocity directions and geometry locations to investigate free molecular flow problems [14]. This treatment is more general than the solid angle treatment [15], which was widely used in studying true collisionless effusion flows with a zero average speed, but it is not applicable to collisionless flows with a nonzero average exit speed. We especially concentrate on density, velocity, temperature, and pressure fields at locations off the cylinder and sphere surfaces.

*Assistant Professor, Department of Mechanical and Aerospace Engineering; ccai@nmsu.edu. Senior Member AIAA.
†Graduate Research Assistant, Ph.D. Candidate, Department of Mechanical and Aerospace Engineering.
‡Research Associate, Department of Mechanical and Aerospace Engineering.
§Assistant Professor, Department of Mechanical and Aerospace Engineering. Senior Member AIAA.

The object surfaces are assumed to be completely diffuse to simplify our study.

This paper is organized as follows. Section II presents some discussions of collisionless gas flows over a cylinder or a sphere. Section III presents some validations with the DSMC simulation results, and Sec. IV concludes this study.

II. Problems and Solutions

This section discusses the problems and solutions for collisionless gas flows over a cylinder or a sphere.

A. Collisionless Flow over a Cylinder

The cylinder problem is illustrated by Fig. 1. A cylinder with a radius $R = 1$ m and wall temperature $T_w = 300$ K is set inside a collisionless gas flow. Collisionless gas, which is assumed to be argon in this study, flows from the left to the right, with a macroscopic average velocity U_0, a temperature of T_0, and a number density of n_0. To aid the study, we assume the outer simulation domain boundary as a circle with a very large radius. At each point on the circle, incoming particles follow a Maxwellian distribution function characterized by the freestream parameters T_0, U_0, and n_0. Suppose there is an arbitrary point $P(x, y)$ which is off the cylinder and we are about to solve for the density, velocity, and temperature fields. In this study, we assume the reflections on the cylinder surface are completely diffuse.

By following the same principles used in our previous study [14,16], we can solve this problem with ease. On the outer boundary large circle, at a point (X, Y), of all particles with a thermal velocity (u, v), only those satisfying the following relation can reach point $P(x, y)$, if (X, Y) is visible from $P(x, y)$:

$$(u + U_0)/(X - x) = v/(Y - y) \qquad (1)$$

If a particle's velocity components satisfy the preceding relation, then it cannot miss passing through $P(x, y)$, unless it is not on the same side of the cylinder as point $P(x, y)$. Because all incoming particles on the large circle follow the freestream Maxwellian distribution function, then, with the preceding relation, the effects of freestream can be described by the velocity space shown on the left side of Fig. 2, within a domain Ω_1. With a similar relation,

$$u/(X - x) = v/(Y - y) \qquad (2)$$

the contributions to point $P(x, y)$ by those diffusely reflected particles from the cylinder are described by an Maxwellian distribution function with a domain Ω_2, shown on the right side of Fig. 2. The boundaries of these two domains, Ω_1 and Ω_2, are determined by point $P(x, y)$, the two specific tangent points $A(Ax, Ay)$ and $B(Bx, By)$, shown in Fig. 1, and the preceding two
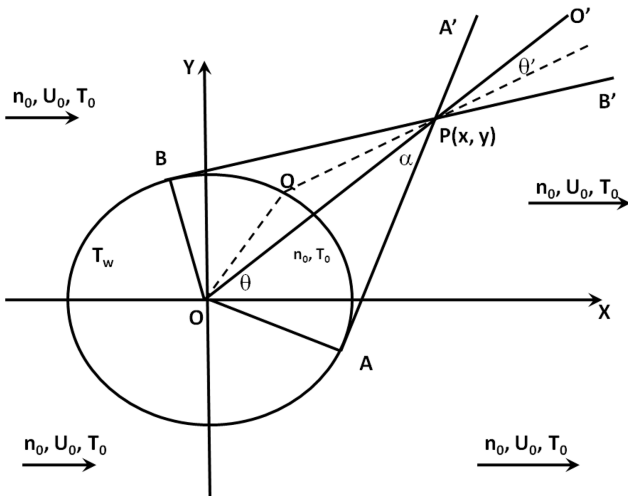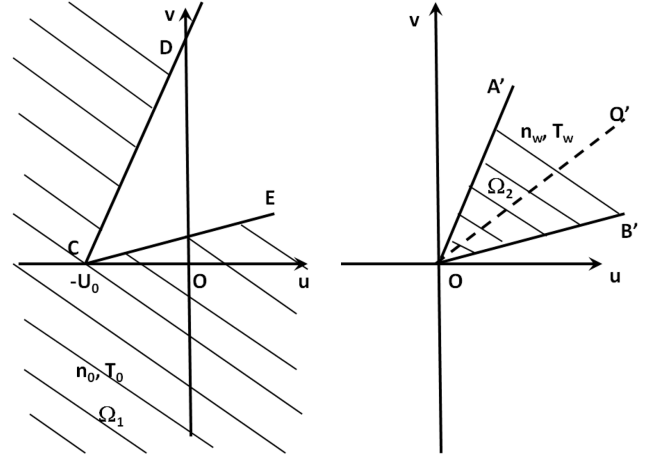

Fig. 2 Typical velocity phase space for the cylinder problem.

equations. If we denote $\theta_2 = \arctan[(y - Ay)/(x - Ax)]$ and $\theta_1 = \arctan[(y - By)/(x - Bx)]$, where $\arctan()$ is a function with a value range of $[-\pi, \pi]$, then from the two equations, $\angle Ecu = \angle B'ou = \theta_1$ and $\angle Dcu = \angle A'ou = \theta_2$. From Eq. (1), we can conclude that point $(-U, 0)$ belongs to domain Ω_1. Hence, the boundaries for Ω_1 and Ω_2 are completely determined by Eqs. (1) and (2). When $U_0 = 0$, then Ω_1 and Ω_2 do not overlap, a combination of these two domains leads to a complete domain where u, v form a full four-quadrant domain.

The velocity distribution function for point $P(x, y)$ consists of contributions from two different Maxwellian distribution functions:

$$f_0(u, v, w) = n_0(\beta_0/\pi)^{3/2} \exp[-\beta_0(u^2 + v^2 + w^2)], \qquad (u, v) \in \Omega_1 \qquad (3)$$

$$f_w(u, v, w) = n_w(\beta_w/\pi)^{3/2} \exp[-\beta_w(u^2 + v^2 + w^2)], \qquad (u, v) \in \Omega_2 \qquad (4)$$

where $\beta_0 = 1/(2RT_0)$, $\beta_w = 1/(2RT_w)$ (following the notation by Gombosi [4]), n_w is not a constant value function,

$$n_w = n_0\sqrt{T_0/T_w}\{\exp(-S^2 S_\alpha^2) + \sqrt{\pi}(SS_\alpha)[1 + \mathrm{erf}(SS_\alpha)]\} \qquad (5)$$

where $S = U_0\sqrt{\beta_0}$ is the speed ratio, and $S_\alpha = -\cos(\alpha)$, α is the angle between freestream and normal direction angle. See the books by Kogan [3] or Bird [6] for details. It can be shown that α and θ have a relation $(R\sin\alpha - y) = (R\cos\alpha - x)\tan\theta$, where $\theta = \angle PoX$. Integrating the preceding two velocity distribution functions, Eqs. (3) and (4), over 1, u, v, $(u^2 + v^2 + w^2)/2$, leads to the macroscopic number density, velocity components, and temperature distributions:

$$\frac{n(x, y)}{n_0} = \frac{\left(\int_{\Omega_1} f_0 \, du \, dv + \int_{\Omega_2} f_w \, du \, dv\right)}{n_0}$$
$$= 1 - \frac{1}{2\pi}\exp(-\beta_0 U_0^2)[(\theta_2 - \theta_1) + \sqrt{\pi}\gamma(\theta_1, \theta_2)]$$
$$+ \frac{1}{2\pi n_0}\int_{\theta_1}^{\theta_2} n_w(\alpha) \, d\theta' \qquad (6)$$

where

$$\gamma(\theta_1, \theta_2)$$
$$= \int_{\theta_1}^{\theta_2} \exp(\beta_0 U_0^2\cos^2\theta)\sqrt{\beta_0}U_0\cos\theta[1 + \mathrm{erf}(\sqrt{\beta_0}U_0\cos\theta)] \, d\theta$$

Fig. 1 Illustration for the cylinder problem.

$$\sqrt{\beta_0}U(x,y) = \frac{1}{n\sqrt{2RT_0}}\left(\int_{\Omega_1}(u+U_0)f_0\,du\,dv + \int_{\Omega_2}uf_w\,du\,dv\right)$$

$$= \frac{n_0U_0}{n\sqrt{2RT_0}} - \frac{n_0\exp(-\beta_0U_0^2)}{2n\pi\sqrt{2RT_0}}$$

$$\times\left[\sqrt{\beta_0}\pi\int_{\theta_1}^{\theta_2}\{U_0^2\cos^3\theta[1+\text{erf}(\sqrt{\beta_0}U_0\cos\theta)]\right.$$

$$\times\exp(\beta_0U_0^2\cos^2\theta)\}\,d\theta$$

$$\left.+\gamma(\theta_1,\theta_2)\frac{\sqrt{\pi}}{2\beta_0U_0}+\frac{U_0(\theta_2-\theta_1)}{2}+\frac{U_0[\sin(2\theta_2)-\sin(2\theta_1)]}{4}\right]$$

$$+\frac{\sqrt{T_w}}{\sqrt{T_0}\pi n(x,y)}\int_{\theta_1}^{\theta_2}\frac{n_w(\alpha)\cos\theta'\,d\theta'}{4} \quad (7)$$

$$\sqrt{\beta_0}V(x,y) = \frac{1}{n\sqrt{2RT_0}}\left(\int_{\Omega_1}vf_0\,du\,dv + \int_{\Omega_2}vf_w\,du\,dv\right)$$

$$= -\frac{n_0}{4\sqrt{\pi}n}\{\exp(-\beta_0U_0^2\sin^2\theta_1)$$

$$\times\cos\theta_1[1+\text{erf}(\sqrt{\beta_0}U_0\cos\theta_1)]-\exp(-\beta_0U_0^2\sin^2\theta_2)$$

$$\times\cos\theta_2[1+\text{erf}(\sqrt{\beta_0}U_0\cos\theta_2)]\}$$

$$+\frac{\sqrt{T_w}}{\sqrt{T_0}\pi n(x,y)}\int_{\theta_1}^{\theta_2}\frac{n_w(\alpha)\sin\theta'\,d\theta'}{4} \quad (8)$$

$$\frac{T(x,y)}{T_0} = \frac{1}{3RnT_0}\left[\int_{\Omega_1}[(u+U_0)^2+v^2+w^2]f_0\,du\,dv\,dw\right.$$

$$\left.+\int_{\Omega_2}(u^2+v^2+w^2)f_w\,du\,dv\right]-\frac{U^2+V^2}{3RT_0}$$

$$= \frac{T_w}{2\pi nT_0}\int_{\theta_1}^{\theta_2}n_w(\alpha)\,d\theta'+\frac{n_0}{n}\left(1+\frac{U_0^2}{3RT_0}\right)$$

$$-\frac{n_0\exp(-\beta_0U_0^2)}{6\pi n(x,y)}\left[3\delta\theta+\frac{U_0^2\delta\theta}{2RT_0}+\frac{U_0^2[\sin(2\theta_2)-\sin(2\theta_1)]}{4RT_0}\right]$$

$$+\frac{n_0}{6nRT_0}\sqrt{\frac{\beta_0}{\pi}}\left[\int_{\theta_1}^{\theta_2}\exp(-\beta_0U_0^2\sin^2\theta)(a^3+2a/\beta_0)\right.$$

$$\left.\times[1+\text{erf}(U_0\cos\theta\sqrt{\beta_0})]\,d\theta\right]-\frac{U^2+V^2}{3RT_0} \quad (9)$$

$$P(x,y)/p_0 = n(x,y)T(x,y)/(n_0T_0) \quad (10)$$

where $\delta\theta = \theta_2-\theta_1$ and $a = -U_0\cos\theta$. It should be pointed out that the results are quite different from our previous study of collisionless flows over a flat plate [16]. Here, the density at the cylinder wall is not a constant, and special attention is needed to obtain correct results. Especially, the integration of $n_w(\theta')$ needs to use the reflection result at the wall. In the right plot of Fig. 2, the velocity phase for point $P(x,y)$ is actually the same as that in Fig. 1, inside $\angle A'PB'$. Hence, the integration of n_w can actually trace back along straight rays back to the cylinder wall, for example, point Q on the wall. The position of Q is determined with a sine angle relation:

$$\sin\theta'/R = \sin\angle OQP/\sqrt{x^2+y^2} \quad (11)$$

and $\angle POQ = \pi - \theta' - \angle OQP$, from which we obtain the position for Q. Then, the wall density $n_w(Q)$ is determined from point P with Eq. (5). Details of the integration processes can be found in our previous work for similar problems [14,16].

When $U_0 = 0$, the density at the wall n_w is a constant, and the preceding results are greatly simplified as

$$n(x,y)/n_0 = 1 + (n_w/n_0-1)(\theta_2-\theta_1)/(2\pi) \quad (12)$$

$$U(x,y) = V(x,y) = 0 \quad (13)$$

$$T(x,y)/T_0 = n_0/n + (T_wn_w/T_0-n_0)(\theta_2-\theta_1)/(2\pi n) \quad (14)$$

B. Collisionless Gas Flows over a Sphere

The problem for a sphere is illustrated with Fig. 3. Suppose, inside the X-Z plane, there is a point $P(X,0,Z)$ off the sphere, with a given collisionless freestream with number density n_0, mean velocity U_0, and static temperature T_0; we are about to compute the density and velocity field at point P. If we suppose $\angle POX = \alpha$, then probably a more convenient way to compute the flowfield is to rotate the axis counterclockwise with a value of $\pi/2 - \alpha$, as shown by Fig. 4. After the computation of the local property at $P'(0,0,\sqrt{X^2+Z^2})$, we rotate back to the original coordinate system. In the rotated system, for point P', the local velocity distribution function consists of two parts:

$$f_0(u,v,w)$$
$$= n_0(\beta_0/\pi)^{3/2}\exp[-\beta_0(u^2+v^2+w^2)], \quad (u,v,w)\in\Omega_1 \quad (15)$$

$$f_w(u,v,w)$$
$$= n_w(\beta_w/\pi)^{3/2}\exp[-\beta_w(u^2+v^2+w^2)], \quad (u,v,w)\in\Omega_2 \quad (16)$$
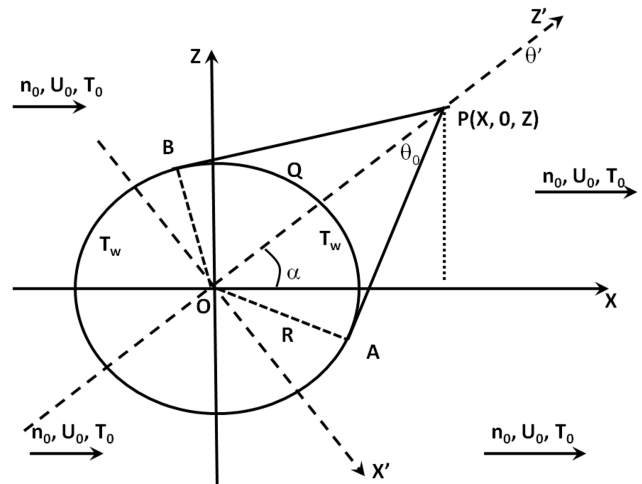

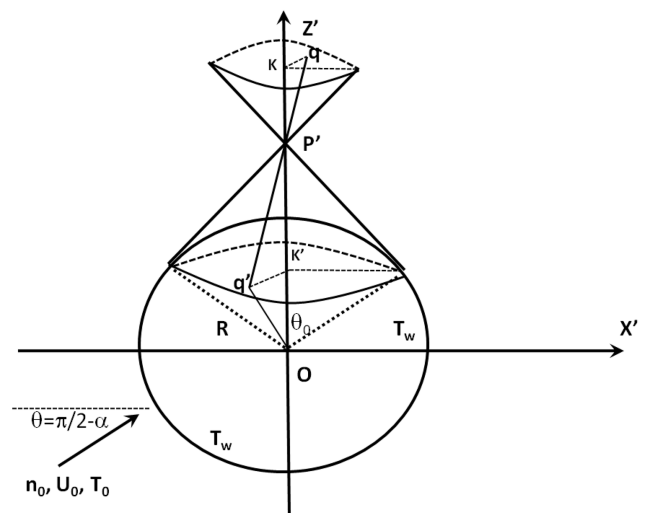**Fig. 3 Illustration for the sphere problem.**

Fig. 4 Sphere problem after a proper rotation.

where $\beta_0 = 1/(2RT_0)$, $\beta_w = 1/(2RT_w)$, Ω_1 and Ω_2 represent the velocity space for freestream and wall shadow regions respectively; n_w in the preceding equation is not constant, and its computation is illustrated with Fig. 4. Ω_2 can be illustrated by the top conical region above point P'; there is one point q with coordinates $r = R'$, $\theta = \theta'$, $\epsilon = \epsilon'$ in the spherical coordinate (r, θ, ϵ), where $0 < \theta < \theta_0$ and $0 < \epsilon < 2\pi$, then the function n_w can trace backward through a ray passing point P' and intersecting the bottom sphere at point q'. With simple geometry relations we can obtain the coordinates for point $q'(oq', \theta, \epsilon + \pi)$: $\angle q'p'O = \theta$, $\sin(\angle P'q'O)/\sqrt{X^2 + Z^2} = \sin(\theta)/R_0$, and $\angle p'Oq' = \pi - \theta - \angle q'p'O$. Based on these fixed co-ordinates, we can compute the normal components (n_x, n_y, n_z) on the sphere for point q'. In the new coordinate system, the flow direction is $(\cos(\pi/2 - \alpha), 0, \sin(\pi/2 - \alpha))$, and we can compute the angle ζ between the freestream and the sphere normal at q': $\cos(\zeta) = [n_x \sin(\alpha) + n_z \cos(\alpha)]$. Then, the density at point q' on the sphere surface is

$$n_w = n_0\sqrt{T_0/T_w}\{\exp(-S^2 S_\zeta^2) + \sqrt{\pi}(S S_\zeta)[1 + \mathrm{erf}(S S_\zeta)]\} \quad (17)$$

where $S_\zeta = -\cos\zeta$.

Integrating the preceding two velocity distribution functions, Eqs. (15) and (16), over $1, u, v, (u^2 + v^2 + w^2)/2$ leads to the macroscopic number density, velocity components, and temperature distributions for the new coordinates:

$$
\begin{aligned}
\frac{n(X', 0, Z')}{n_0} &= \frac{1}{n_0}\left(\int_{\Omega_1} f_0\, \mathrm{d}u\, \mathrm{d}v\, \mathrm{d}w + \int_{\Omega_2} f_w\, \mathrm{d}u\, \mathrm{d}v\, \mathrm{d}w\right) \\
&= 1 - 1\left(\frac{\beta_0}{\pi}\right)^{3/2}\int_0^{2\pi}\mathrm{d}\epsilon\int_0^{\theta_0}\sin\phi\,\mathrm{d}\phi\left[\frac{U_0 a}{2\beta_0}\exp(-\beta_0 U_0^2 a^2)\right. \\
&\quad \left. + \frac{1}{2}\left(U_0^2 a^2 + \frac{1}{2\beta_0}\right)\sqrt{\frac{\pi}{\beta_0}}[1 + \mathrm{sign}(U_0 a)\mathrm{erf}(U_0|a|\sqrt{\beta_0})]\right] \\
&\quad \times \exp[-\beta_0 U_0^2(1-a^2)] + \frac{1}{4\pi n_0}\int_0^{2\pi}\mathrm{d}\epsilon\int_0^{\theta_0} n_w\sin\phi\,\mathrm{d}\phi \quad (18)
\end{aligned}
$$

where

$$a = \sin\phi\cos\epsilon\cos(\pi/2 - \alpha) + \cos\phi\sin(\pi/2 - \alpha)$$

$$
\begin{aligned}
&\sqrt{\beta_0}U'(X', 0, Z') \\
&= \frac{1}{n\sqrt{2RT_0}}\left\{\int_{\Omega_1}\left[u + U_0\cos\left(\frac{\pi}{2} - \alpha\right)\right]f_0\,\mathrm{d}u\,\mathrm{d}v\,\mathrm{d}w\right. \\
&\quad \left. + \int_{\Omega_2} u f_w\,\mathrm{d}u\,\mathrm{d}v\,\mathrm{d}w\right\} \\
&= \frac{n_0 U_0\sin\alpha}{n\sqrt{2RT_0}} - \left(\frac{\beta_0}{\pi}\right)^{3/2}\frac{n_0}{n}\int_0^{2\pi}\mathrm{d}\epsilon\int_0^{\theta_0} \\
&\quad \times \left[K\left(\frac{b^2}{2\beta_0} + \frac{1}{2\beta_0^2}\right) - \frac{3b^2 K}{2\beta_0}\exp(-\beta_0 b^2)\right. \\
&\quad + \left(-\frac{3bK}{2\beta_0} - b^3 K\right)\sqrt{\frac{\pi}{\beta_0}}[1 + \mathrm{sign}(U_0 a)\mathrm{erf}(U_0|a|\sqrt{\beta_0})] \\
&\quad \left. + \frac{3b^2 K}{2\beta_0}\exp(-\beta_0 b^2)\right]\exp[-\beta_0 U_0^2(1-a^2)]\,\mathrm{d}\theta \\
&\quad + \frac{1}{2\pi n\sqrt{\pi}}\sqrt{\frac{T_w}{T_0}}\int_0^{\theta_0}\sin^2\phi\cos\phi\,\mathrm{d}\phi\int_0^{2\pi} n_w(\theta', \epsilon)\,\mathrm{d}\epsilon \quad (19)
\end{aligned}
$$

where $K = \sin^2\theta\cos\epsilon$ and $b = -U_0 a$.

$$
\begin{aligned}
&\sqrt{\beta_0}W'(X', 0, Z') \\
&= \frac{1}{n\sqrt{2RT_0}}\left\{\int_{\Omega_1}\left[v + U_0\sin\left(\frac{\pi}{2} - \alpha\right)\right]f_0\,\mathrm{d}u\,\mathrm{d}v\,\mathrm{d}w\right. \\
&\quad \left. + \int_{\Omega_2} w f_w\,\mathrm{d}u\,\mathrm{d}v\,\mathrm{d}w\right\} \\
&= \frac{n_0 U_0\cos\alpha}{n\sqrt{2RT_0}} - \left(\frac{\beta_0}{\pi}\right)^{3/2}\frac{n_0}{n}\int_0^{2\pi}\mathrm{d}\epsilon\int_0^{\theta_0} \\
&\quad \times \left[J\left(\frac{b^2}{2\beta_0} + \frac{1}{2\beta_0^2}\right) - \frac{3b^2 J}{2\beta_0}\exp(-\beta_0 b^2)\right. \\
&\quad + \left(-\frac{3bJ}{2\beta_0} - b^3 J\right)\frac{1}{2}\sqrt{\frac{\pi}{\beta_0}}[1 + \mathrm{sign}(U_0 a)\mathrm{erf}(U_0|a|\sqrt{\beta_0})] \\
&\quad \left. + \frac{3b^2 J}{2\beta_0}\exp(-\beta_0 b^2)\right]\exp[-\beta_0 U_0^2(1-a^2)]\,\mathrm{d}\theta \\
&\quad + \frac{1}{2n\pi\sqrt{\pi}}\sqrt{\frac{T_w}{T_0}}\int_0^{\theta_0}\sin\phi\cos\phi\int_0^{2\pi} n_w(\theta', \epsilon)\,\mathrm{d}\epsilon\,\mathrm{d}\phi \quad (20)
\end{aligned}
$$

where $J = \sin^2\theta\cos\theta$. With a known value of $U(X', 0, Z')$ and $W(X', 0, Z')$, we can rotate the vector counterclockwise with an angle $\pi/2 - \alpha$:

$$
\begin{aligned}
&U(X, 0, Z) \\
&= U'(X', 0, Z')\cos(\pi/2 - \alpha) + W'(X', 0, Z')\sin(\pi/2 - \alpha) \quad (21)
\end{aligned}
$$

$$
\begin{aligned}
&W(X, 0, Z) \\
&= U'(X', 0, Z')\sin(\pi/2 - \alpha) - W'(X', 0, Z')\cos(\pi/2 - \alpha) \quad (22)
\end{aligned}
$$

The temperature field is

$$
\begin{aligned}
\frac{T(X, 0, Z)}{T_0} &= \frac{1}{3RnT_0}\left[\int_{\Omega_1}\{[u + U_0\cos(\pi/2 - \alpha)]^2 + v^2\right. \\
&\quad + [w + U_0\sin(\pi/2 - \alpha)]^2\}f_0\,\mathrm{d}u\,\mathrm{d}v\,\mathrm{d}w \\
&\quad \left. + \int_{\Omega_2}(u^2 + v^2 + w^2)f_w\,\mathrm{d}u\,\mathrm{d}v\right] - \frac{U^2 + W^2}{3RT_0} \\
&= \frac{T_w}{4\pi n T_0}\int_0^{2\pi}\mathrm{d}\epsilon\int_0^{\theta_0}\sin\theta' n_w\,\mathrm{d}\theta' + \frac{n_0}{n}\left(1 + \frac{U_0^2}{3RT_0}\right) \\
&\quad - \frac{1}{3RT_0}\int_0^{2\pi}\mathrm{d}\epsilon\int_0^{\theta_0}\sin\theta' n_w\left(\frac{\beta_0}{\pi}\right)^{3/2} \\
&\quad \times \exp[-\beta_0 U_0^2(1-a^2)]\left[\left(-\frac{5b}{4\beta_0^2} - \frac{b^3}{2\beta_0}\right)\exp(-\beta_0 b^2)\right. \\
&\quad \left. + \left(\frac{3}{4\beta^2} + b^4 + \frac{3b^2}{\beta_0}\right)[1 - \mathrm{sign}(b)\mathrm{erf}(|b|\sqrt{\beta_0})]\right]\mathrm{d}\theta' \\
&\quad - \frac{U^2 + W^2}{3RT_0} \quad (23)
\end{aligned}
$$

Even though the preceding two sets of solutions are very complex and semi-analytical, they are exact solutions to real physical problems. Further, the evaluation speed via a computer can be very fast when compared to DSMC simulations via the same computer.

III. Validations

In the previous section, we present the exact solutions for collisionless gas flows over a cylinder and a sphere. The next natural step is to validate these solutions with numerical simulations. We perform two numerical simulations with a DSMC package named GRASP which is being developed at New Mexico State University. We must emphasize that this paper is not devoted to advocate the DSMC method and the GRASP package is not developed solely for this study. We choose the sphere and cylinder diameters as the

characteristic length for the Knudsen number. In general, the freestream number density determines the Kn number, and in this study, we choose the freestream number density to achieve a Kn number 10^3. However, in these simulations, the collision functions inside GRASP are turned off. As such, true collisionless gas flows are guaranteed.

The freestream flow is chosen to be argon, with a static temperature $T_0 = 200$ K, and the wall temperature is set to $T_w = 300$ K. The cylinder and sphere radii are set to 1 m, whereas the outer radii for the simulation domain are set to 4 and 2.5 m with a total number of 100×100 cells, mainly to provide a high resolution. As for the number of particles to be used, some past studies suggest using a specific number of particles, for example, 20 particles per cell [17,18]. In this study, we use about 5 million particles in each of these simulations. The time step is chosen based on the grid size and the average freestream velocity; on average, particles shall move one cell during one time step. The outer domain is set to inlet boundary conditions. When a particle collides at the inlet boundary from the simulation domain, it is removed from the simulation; meanwhile, within each time step, a certain number of new particles are injected into the outer inlet boundaries, and the particles' velocities are assigned by sampling from a Maxwellian distribution function. This treatment is perfectly consistent with the outer boundary treatment for the analytical solution study in the previous section. For the two test cases in this study, we choose the following freestream mean velocity: $S = \sqrt{\beta_0} U_0 = 0.5$.

Figures 5–9 show the results of normalized number density, velocity components, temperature, and pressure for the cylinder case. Macroscopic properties of higher-order moments of the distribution functions are neglected here for simplicity, even though, in principal, they are computable with more complex relations. The top contours with solid lines are analytical results, and the bottom are DSMC simulation results. The flow patterns for this test case are very complex indeed: a source at the front tip and a sink at the rear tip are visible, the nonzero freestream pushes the contour lines backward, and these flow patterns are exactly symmetric about the X axis. In the U-velocity contours, the highest velocity spot is off the cylinder surface, and it is different from the corresponding potential flow result. These contours show excellent agreement between the analytical and numerical results, and we can confidently conclude that they accurately represent physical results. It is very evident that the contours have very complex patterns. The analytical solutions include factors from geometry relations, the freestream number density n_0, mean velocity U_0, temperature T_0, and wall temperature T_w.

Figures 10–13 show the results of normalized number density, velocity components, and temperature for the sphere case. In general, the analytical and numerical results are essentially identical. It is also evident that, at the same location as the cylinder case, the number density value in the sphere case is smaller. This is because gas is
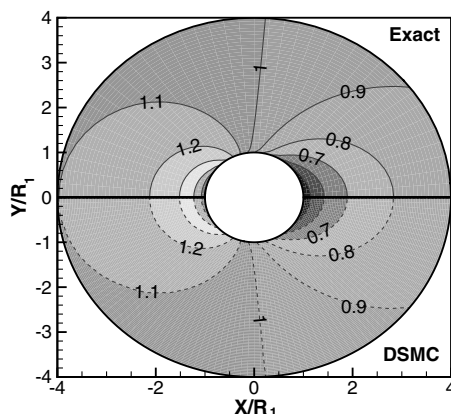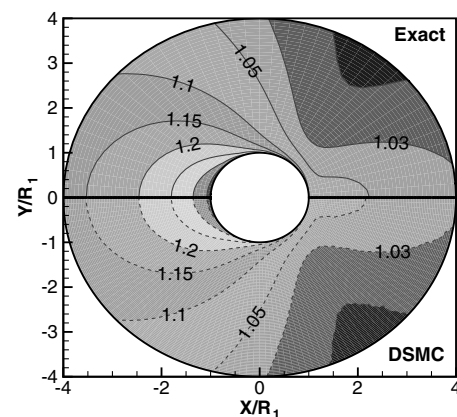

Fig. 5 Case A: contours of normalized number density for the cylinder problem, $S = U_0/\sqrt{2RT_0} = 0.5$, $T_0 = 200$ K, $T_w = 300$ K (solid line: analytical; dashed line: DSMC).
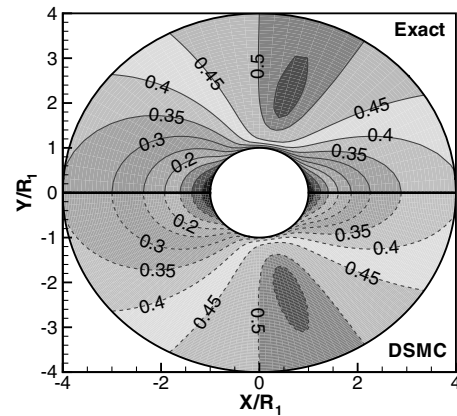
Fig. 6 Case A: contours of normalized U velocity for the cylinder problem, $S = U_0/\sqrt{2RT_0} = 0.5$, $T_0 = 200$ K, $T_w = 300$ K (solid line: analytical; dashed line: DSMC).
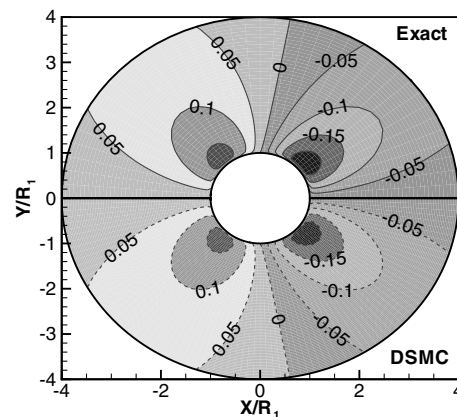
Fig. 7 Case A: contours of normalized V velocity for the cylinder problem, $S = U_0/\sqrt{2RT_0} = 0.5$, $T_0 = 200$ K, $T_w = 300$ K (solid line: analytical; dashed line: DSMC).

Fig. 8 Case A: contours of normalized temperature for the cylinder problem, $S = U_0/\sqrt{2RT_0} = 0.5$, $T_0 = 200$ K, $T_w = 300$ K (solid line: analytical; dashed line: DSMC).

much easier to flow around the sphere, whereas the cylinder is more effective to block gas molecules.

It is also meaningful to compare some past results of centerline density distribution in the literature, because of its important application in space engineering. For the back and ram sides of a spherical spacecraft, there are some simple formulas [19] for the centerline density distributions:
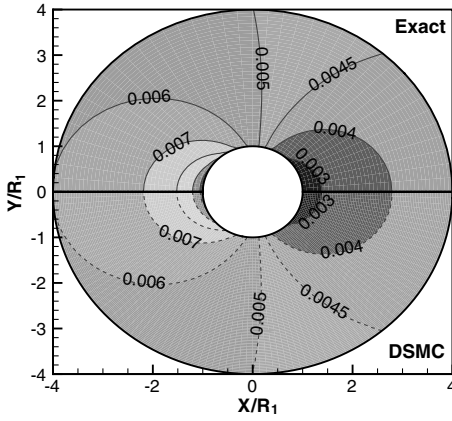
Fig. 9   Case A: contours of normalized pressure for the cylinder problem, $S = U_0/\sqrt{2RT_0} = 0.5$, $T_0 = 200$ K, $T_w = 300$ K (solid line: analytical; dashed line: DSMC).
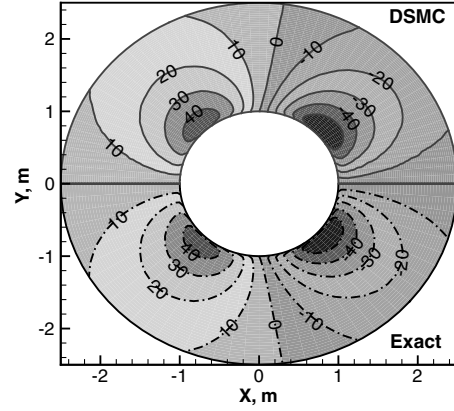

Fig. 12   Case B: contours of V velocity, in meters per second, for the sphere problem, $S = U_0/\sqrt{2RT_0} = 0.5$, $T_0 = 200$ K, $T_w = 300$ K (dashed line: analytical; solid line: DSMC).
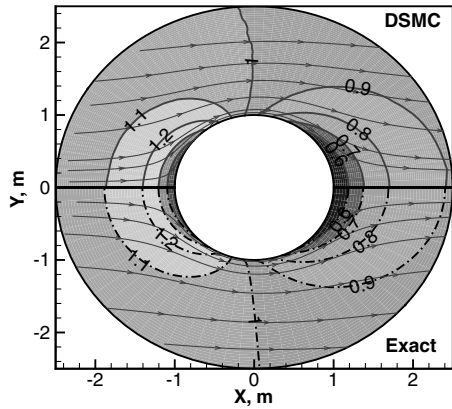

Fig. 10   Case B: normalized density contours for the sphere problem, $S = U_0/\sqrt{2RT_0} = 0.5$, $T_0 = 200$ K, $T_w = 300$ K (solid line: DSMC; dashed lines: analytical).
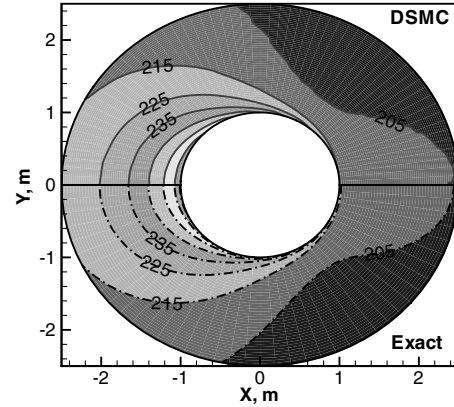

Fig. 13   Case B: contours of temperature, in Kelvin, for the sphere problem, $S = U_0/\sqrt{2RT_0} = 0.5$, $T_0 = 200$ K, $T_w = 300$ K (dashed line: analytical; solid line: DSMC).
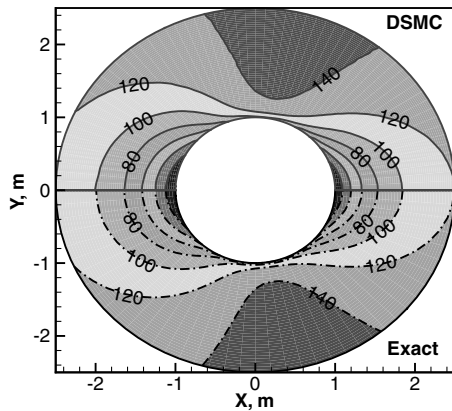
streams, assuming the reflections on the spherical object are completely reflective. However, for locations close to the sphere, the preceding equations are not accurate. Equation (18) provides more accurate centerline density distributions:

$$\frac{n(X,0,0)}{n_0}$$
$$= 1 - \frac{1}{2}\{1 - \mathrm{erf}(S) - \exp(-S^2\sin^2\theta_0)\cos\theta_0[1 - \mathrm{erf}(S\cos\theta_0)]\}$$
$$+ \frac{1}{2}\sqrt{\frac{T_0}{T_w}}\int_0^{\theta_0} n_w(\zeta)\sin\theta\,\mathrm{d}\theta, \qquad X < 0 \qquad (25)$$

$$\frac{n(X,0,0)}{n_0}$$
$$= 1 - \frac{1}{2}\{1 + \mathrm{erf}(S) - \exp(-S^2\sin^2\theta_0)\cos\theta_0[1 + \mathrm{erf}(S\cos\theta_0)]\}$$
$$+ \frac{1}{2}\sqrt{\frac{T_0}{T_w}}\int_0^{\theta_0} n_w(\zeta)\sin\theta\,\mathrm{d}\theta, \qquad X > 0 \qquad (26)$$

where θ_0 is the largest semisolid angle subtended by the sphere from point $(X,0,0)$, that is, $\theta_0 = \arcsin(R_0/X)$. When X is infinitely far from the sphere, $\theta_0 = 0$; when X is infinitely close to the sphere, $\theta_0 = \pi/2$.

Figure 14 shows a comparison of the analytical solutions of Eqs. (25) and (26), DSMC, and Eq. (24), with $S = 0.5$. The DSMC simulation results are extracted from Fig. 10. As we can see, the

Fig. 11   Case B: contours of U velocity, in meters per second, for the sphere problem, $S = U_0/\sqrt{2RT_0} = 0.5$, $T_0 = 200$ K, $T_w = 300$ K (dashed line: analytical; solid line: DSMC).

$$n(X,0,0) = \begin{cases} n_0[1 - U_0^2\beta_0(\frac{R_0}{X})^2], & X > R_0; \\ n_0[1 + \frac{R_0^2}{(2|X|-R_0)^2}], & X < -R_0 \end{cases} \qquad (24)$$

where R_0 is the sphere radius, the first equation is for the backside, and the second equation is for the front side, or well known as the ram side. These simple expressions provide accurate estimations for density distributions at far field for cases with hypervelocity free-
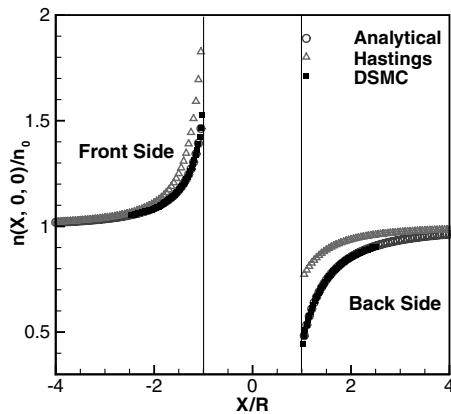
Fig. 14 Normalized centerline density distribution, $S = 0.5$, $T_0 = 200$ K, $T_w = 300$ K.

DSMC and analytical results agree well. The results from Eq. (24), however, show large discrepancy at locations very close to the sphere surface. Figure 15 shows another comparison for the case of $S = 2.0$ with larger discrepancy; Eq. (24) even provides negative density value at the back stagnation point. Even though Eq. (24) has a very simple format, we need to keep in mind that it is an approximation, only valid at locations far from the object. There are several obvious limitations in Eq. (24) as well. For the ram side, in general, at different locations along the centerline, the density is a function of the freestream mean velocity U_0, but Eq. (24) does not include any factor of freestream velocity. Also, Eq. (24) predicts that, on the front stagnation point of the sphere, the normalized density ratio is a fixed value of 2.0 regardless of the freestream velocity. This is not accurate here because of two reasons related to Eq. (17). First, if the freestream mean velocity is not large enough, then only a fraction of the freestream particles can reach the front stagnation point. Those with thermal velocity components $u < -S\sqrt{\beta_0}$ cannot reach the front stagnation point. Second, for completely diffuse wall reflections, the temperature ratio $\sqrt{T_0/T_w}$ is a key factor in determining n_w according to Eq. (17). These two factors accurately result in different normalized number density values at the stagnation point for different cases.

It is worth mentioning that the evaluations for the exact solutions only take less than 1 min, whereas the DSMC simulations require several days with the same computer. Plus, all geometry factors and freestream factors clearly display in the exact solutions.

Before we forward to the conclusion section, we would like to comment on the impact of these results. For highly rarefied internal gas flows inside an enclosure, our recent work indicates that we can use the collisionless exact solutions as base solutions to approximate the solutions for high-Kn number cases; and as long as Kn is larger
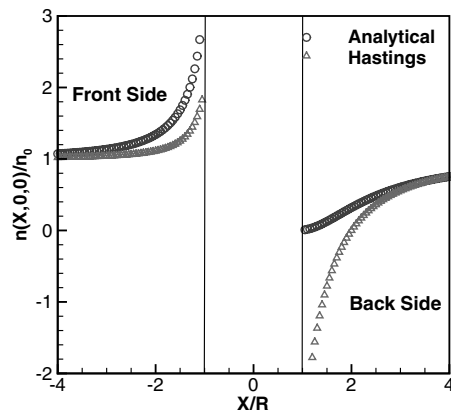
than 1.0, the approximate solutions for the heat flux rate, flow, and thermal fields are fairly accurate. This is because, without strong gradients, high-Kn number flow essentially means that there are not many collisions involved; those collisions are the reasons for the flow to deviate from the collisionless flow situation. For highly rarefied external gas flows, we believe that we can use the corresponding analytical exact solutions of collisionless flows as the first-order approximations as well. Hence, those exact solutions, even though with complex expressions, have important and practical potential applications. However, how well these approximations perform is really not the major concern of this paper; we shall report on this soon in a future study. Especially, we need to provide many validation cases with different combinations of Mach and Kn numbers for external gas flows, and some test cases may involve shock waves.

IV.　Conclusions

We have reported a study of collisionless flows over a cylinder or a sphere by applying some general gas-kinetic evaluation procedures. These collisionless flows have very complex density, velocity, and temperature patterns. The almost identical agreement between the analytical and DSMC simulation results indicates the approach we used in this study is correct.

This study complements many analytical studies on the drag and heat transfer rates for a cylinder or a sphere in collisionless gas flows. Even though the solution expressions are very complex and need to be evaluated with a computer, they are exact, and different factors from the freestream and the wall surface are clearly displayed. There are many numerical simulation results in the literature, however, this is probably the first time the exact solutions are accurately presented. Evaluating these solutions is much faster than simulating the flow-field with the DSMC method.

The approach used in this study is general and very heuristic, and can be used to study other collisionless external flows over objects of different geometries. Further, these results may be used as base solutions to solve for less rarefied flow situations.

References

[1] Liu, C. Y., "Part II. Kinetic Theory Description of Conductive Heat Transfer from a Fine Wire," Ph.D. Dissertation, California Inst. of Technology, Pasadena, CA, 1962.
[2] Epstein, P. S., "Zur Theorie des Radiometers," *Zeitschrift fuer Physik*, Vol. 54, Nos. 7–8, 1929, pp. 537–563.
doi:10.1007/BF01338485
[3] Kogan, M. N., *Rarefied Gas Dynamics*, Plenum Press, New York, 1969.
[4] Gombosi, T. I., *Gaskinetic Theory*, Cambridge Univ. Press, New York, 1994.
[5] Shen, C., *Rarefied Gas Dynamics: Fundamentals, Simulations and Micro Flows*, Springer, New York, 2005.
[6] Bird, G. A., *Molecular Gas Dynamics and the Direct Simulation of Gas Flows*, 2nd ed., Claredon, Oxford, England, U.K., 1994.
[7] Chen, X., *Gaskinetics and Its Applications in Heat Transfer and Flows*, Tsinghua Univ. Press, Beijing, 1996.
[8] Sone, Y., "Flows Induced by Temperature Fields in a Rarefied Gas and Their Ghost Effect on the Behavior of a Gas in the Continuum Limit," *Annual Review of Fluid Mechanics*, Vol. 32, Jan. 2000, pp. 779–811.
doi:10.1146/annurev.fluid.32.1.779
[9] Loth, E., "Compressibility and Rarefaction Effects on Drag of a Spherical Particle," *AIAA Journal*, Vol. 46, No. 9, 2008, pp. 2119–2228.
[10] Wang, M., and Li, Z., "Similarity of Ideal Gas Flow at Different Scales," *Science in China: Series E*, Vol. 46, No. 6, Dec. 2003, pp. 661–670.
doi:10.1360/02ye0072
[11] Delgado-Buscalioni, R., and Coveney, P. V., "Continuum-Particle Hybrid Coupling for Mass, Momentum, and Energy Transfers in Unsteady Fluid Flow," *Physical Review E (Statistical Physics, Plasmas, Fluids, and Related Interdisciplinary Topics)*, Vol. 67, No. 4, 2003, pp. 046704.
doi:10.1103/PhysRevE.67.046704
[12] Wang, M., and Li, Z., "An Enskog Based Monte Carlo Method for High Knudsen Number Non-Ideal Gas Flows," *Computers & Fluids*, Vol. 36, No. 8, Sept. 2007, pp. 1291–1297.
doi:10.1016/j.compfluid.2006.12.006
[13] Pan, N., "Modeling and Prediction of the Effective Thermal Conductivity of Random Open-Cell Porous Foams," *International Journal of*

Fig. 15 Normalized centerline density distribution, $S = 2.0$, $T_0 = 200$ K, $T_w = 300$ K.

Heat and Mass Transfer, Vol. 51, Nos. 5–6, Jan. 2008, pp. 1325–1331.
doi:10.1016/j.ijheatmasstransfer.2007.11.031

[14] Cai, C., and Boyd, I. D., "Theoretical and Numerical Study of Free-Molecular Problems," *Journal of Spacecraft and Rockets*, Vol. 44, No. 3, 2007, pp. 619–624.
doi:10.2514/1.25893

[15] Narasimha, R., "Orifice Flow of High Knudsen Number," *Journal of Fluid Mechanics*, Vol. 10, No. 3, 1961, p. 371.
doi:10.1017/S0022112061000986

[16] Cai, C., and Khasawneh, K. R., "Collisionless Gas Flows over a Flat Cryogenic Pump Plate," *Journal of Vacuum Science and Technology, A: Vacuum, Surfaces, and Films*, Vol. 27, No. 4, July–Aug. 2009, pp. 601–610.
doi:10.1116/1.3125266

[17] Boyd, I., Chen, G., and Candler, G., "Predicting Failure of the Continuum Fluid Equations in Transitional Hypersonic Flows," *Physics of Fluids*, Vol. 7, No. 1, 1995, p. 210.
doi:10.1063/1.868720

[18] Wang, M., and Li, Z., "Gas Mixing in Microchannels Using the Direct Simulation Monte Carlo Method," *International Journal of Heat and Mass Transfer*, Vol. 49, Nos. 9–10, 2006, pp. 1696–1702.
doi:10.1016/j.ijheatmasstransfer.2005.10.022

[19] Hastings, D., and Garrett, H., *Spacecraft-Environment Interactions*, Cambridge Univ. Press, New York, 1996.

I. Boyd
Associate Editor